Engineered Contrast Agents in a Single Structure for T_1-T_2 Dual Magnetic Resonance Imaging†

Alejandro Cabrera-García,[a] Elisa Checa-Chavarria,[b] Jesús Pacheco-Torres,[c] Ángela Bernabeu-Sanz,[d] Alejandro Vidal-Moya,[a] Eva Rivero-Buceta,[a] Germán Sastre,[a] Eduardo Fernández,[b] and Pablo Botella[a,*]

[a] *Instituto de Tecnología Química, Universitat Politècnica de València-Consejo Superior de Investigaciones Científicas, Avenida de los Naranjos s/n, 46022 Valencia, Spain*

[b] *Instituto de Bioingeniería, Universidad Miguel Hernández, Elche, Spain and Centro de Investigación Biomédica en Red (CIBER-BBN), Spain*

[c] *Unidad de Resonancia Magnética Funcional, Instituto de Neurociencias (CSIC-UMH), Alicante, Spain*

[d] *Unidad de Resonancia Magnética, Inscanner S.L., Alicante, Spain*

* To whom correspondence should be addressed. E-mail: pbotella@itq.upv.es. Fax: +34 96 3879444.

†Electronic Supporting Information (ESI) available: Additional tables and figures on material characterization and relaxivity values.

Abstract

The development of contrast agents (CAs) for Magnetic Resonance Imaging (MRI) with T_1-T_2 dual-mode relaxivity requires the accurate assembly of T_1 and T_2 magnetic centers in a single structure. In this context, we have synthesized a novel hybrid material by monitoring the formation of Prussian Blue analogue $Gd(H_2O)_4[Fe(CN)_6]$ nanoparticles with tailored shape (from nanocrosses to nanorods) and size, and further protection with a thin and homogeneous silica coating through hydrolysis and polymerization of silicate at neutral pH. The resulting $Gd(H_2O)_4[Fe(CN)_6]@SiO_2$ magnetic nanoparticles are very stable in biological fluids. Interestingly, this combination of Gd and Fe magnetic centers closely packed in the crystalline network promotes a magnetic synergistic effect, which results in significant improvement of longitudinal relaxivity with regards to soluble Gd^{3+} chelates, whilst keeping the high transversal relaxivity inherent to the iron component. As a consequence, this material shows excellent activity as MRI CA, improving positive and negative contrast in T_1- and T_2- weighted MR images, both in *in vitro* (e.g., phantom) and *in vivo* (e.g., Sprague-Dawley rats) models. In addition, this hybrid shows a high biosafety profile and has strong ability to incorporate organic molecules on surface with variable functionality, displaying great potential for further clinical application.

Keywords: Core-Shell Hybrid, Magnetic Nanoparticles, Prussian Blue Analogue, Silica Coating, Dual Magnetic Resonance Imaging, Contrast Agent.

Introduction

Magnetic resonance imaging (MRI) is a powerful and thoroughly used non-invasive and non-radioactive technique for clinical diagnostic that can provide information on the anatomy, function and metabolism of tissues *in vivo*.[1-5] In ^{1}H-MRI, Signal Intensity (SI) depends on a combination of factors including proton density, longitudinal (T_1) and transversal (T_2) relaxivity times and the microenvironment (cell density, pH, oxygenation). Unfortunately, the intrinsic contrast provided by these factors and associated changes due to a pathologic condition are often too limited to enable a sensitive and accurate diagnosis. For that reason, there is an increased use of MRI contrast agents (CA) that improve image resolution based on their selective accumulation in the Region Of Interest (ROI).[6] Based on their relaxation activity, these CAs are classified as positive (T_1-weighted) or negative (T_2-weighted) image contrast promoters. All clinically approved MRI T_1 CAs are based on paramagnetic Gd^{3+} soluble chelates with polyamino-polycarboxylate ligands,[7,8] due to their strong paramagnetic activity. However, the use of Gd^{3+} solutions involves some technical issues and health risks that limit imaging performance. Here, the quick renal filtration indicates a poor pharmacokinetic profile, reducing sensitivity, increasing scanning time, and imposing the administration of high Gd^{3+} doses,[9] which may lead to toxicity effects, such as headache, nausea, dizziness and nephrogenic systemic fibrosis.[10-12] On the other hand, current T_2 CAs in clinical practice are based on superparamagnetic iron oxide nanoparticles (SPIONs),[13] which produce T_2 shortening, providing negative contrast. However, this is hardly seen in low signal body regions, and it may be confused with hemorrhages, calcification, fat, blood clots and other possible artifacts in damaged tissue, which lowers their interest in clinical diagnosis.

At this point, the acquisition of MRI weighted in T_1 and T_2 could improve the safety of diagnosis and cross-validate the possible false-positive information.[14] T_1-T_2 dual-modal strategy can provide complementary T_1 and T_2 MRI images, making it possible to isolate artifact signals from the contrast agents in the ROI.[15] An ideal T_1-T_2 dual-modal MRI acquisition is desirable for tissues with moderate T_1 and T_2 relaxation times, such as liver, kidneys, muscle and brain matter.[12] Actually, some nanoparticles present unique characteristics that allow exploiting the T_1-T_2 dual-mode CA concept. Several strategies have been proposed for the development of these materials. The simplest way is the direct conjugation of T_1 elements (e.g., Gd or Mn-containing systems) and T_2 elements (e.g., SPIONs). For instance, Gd-chelates can be covalently coupled over the surface of SPIONs,[16] although this usually results in low gadolinium loading; not to mention the fact that metal leaching in physiological fluids may be an issue. Alternatively, a hybrid system of T_1 and T_2 elements can be prepared by assembling gadolinium oxide and iron nanoparticles in a core-shell layout structure.[17] Unfortunately, interferences are usual, as magnetic coupling induced by close T_2/T_1 structures trends to undesirable quenching of both T_2 and T_1 signals in MRI.[18] In these cases, a silica separating layer inserted between the T_2 magnetic nanoparticle (core) and the T_1 contrast material (shell) allows for a fine separation distance control, which can minimize the perturbation of T_2 signal over the T_1 contrast effect.[19] However, although the SiO_2 layer between the T_2 core and T_1 shell may attenuate magnetic coupling, it also reduces the magnetic field to surrounding water molecules, leading to strong T_2 signal reduction.[20] Conversely, it is possible to minimize T_1 and T_2 signal coupling by monitoring the incorporation of Gd^{3+} into iron nanoparticles. Here, composites obtained by embedding gadolinium oxide crystals into iron nanoparticles,[21] or

by synthesis of "Janus" nanoparticles with both components,[20] have shown improved magnetic properties, with a synergistic action between T_1 and T_2 centers that enhance contrast effects in MR imaging. Moreover, a similar cooperative effect has been reported by doping SPIONs with Mn^{2+} ions.[22]

In this context, it has been reported that Prussian Blue (PB) analogues doped with Gd^{3+}, with general molecular formula $K_xGd_{1-x}(H_2O)_n[Fe(CN)_6]$ and nanosized crystallites, may present high performance as dual T_1-T_2 contrast agents.[23,24] In these materials, T_1 and T_2 magnetic centers are located in the same crystalline framework, very close to each other. Also, Mn-doped PB has been proposed as CA with ultrahigh longitudinal relaxivity.[25] The local magnetic field induced by the superparamagnetic Fe centers promotes Gd spins alignment in the same direction, resulting in a boost of T_1 contrast effect[21,26] which, gathered with the strong T_2 contrast activity associated to Fe atoms, may promote a mastered combination of magnetic centers in the same network for dual-modal MRI. Unfortunately, and despite the good relaxivity results obtained in *in vitro* studies, the clinical use of PB derivatives as MRI CAs is precluded by their partial solubility in aqueous medium at physiological pH, releasing toxic quantities of both Gd and Fe ions. This situation, nevertheless, could be skipped if Gd-containing PB nanoparticles are protected with a stable and diamagnetic thin silica coating. This is not possible in alkaline medium, as PB and its analogs react with soluble silicate, triggering an ion exchange process which results in complete iron exchange and stoichiometric condensation of gadolinium hydroxide and silica, to give $Gd(OH)_3{\cdot}3SiO_2.xH_2O$ composite.[27,28] Herein, we have successfully carried out the coating of PB derivative $Gd(H_2O)_4[Fe(CN)_6]$ nanoparticles by polymerizing the silicate at neutral pH. For this purpose, we have optimized a biomimetic synthetic strategy

developed by our group to activate silica at pH~7 by using functional mimics of the protein silicatein α (e.g., triethylamine, TEA)[29] as catalyst. By stepwise control of $Gd(H_2O)_4[Fe(CN)_6]$ preparation and subsequent silane hydrolysis and polymerization, we have obtained hybrid material $Gd(H_2O)_4[Fe(CN)_6]@SiO_2$ nanoparticles, very stable in biological fluids, with tailored shape (from nanocrosses to nanorods) and size. By combining Gd and Fe magnetic centers closely packed in the same crystalline structure a magnetic synergistic effect is imposed by Fe atoms over Gd sites, which leads to strong increase of longitudinal relaxivity, whilst keeping the high transversal relaxivity corresponding to Fe centers. This results in a CA with constant Gd:Fe atomic ratio able to improve positive and negative contrast in T_1- and T_2- weighted MR images, both in *in vitro* (e.g., phantom) and *in vivo* (e.g., Sprague-Dawley rats) systems. Furthermore, this material shows low cytotoxicity in cell culture studies and no structural or cellular abnormalities in histological sections, and the silica coating is easy to functionalize with organic groups, displaying great potential for clinical MRI.

Experimental

Reagents, cells and animals

All reagents were purchased from Sigma-Aldrich, except for $Gd(NO_3)_3.6H_2O$, (3-cyanopropyl)trimethoxysilane (CPTMS) (ABCR), tetramethyl orthosilicate (TMOS) (MERCK), 2,5,8,11-Tetraoxatetradecan-14-oic acid succinimidyl ester (PEG_3) (Iris Biotech) and HPLC grade solvents (Scharlab).

HeLa cell line, 3T3 (fibroblasts cells), 42-MG-BA (glioblastoma multiforme cells) and SH-SY5Y (neuroblastoma cells), were purchased from German Collection of Microorganisms

and Cell Cultures, Braunschweig, Germany. Reagents used for cells growth were MEM (Earle's), RPMI Medium 1640, DMEM and Ham (F12) Nut MIX (Gibco BRL-Life Technologies, CA, USA) fetal bovine serum (FBS) and penicillin/streptomycin solution (Pen-Strep). Dimethyl sulfoxide (DMSO) and 3-(4,5-dimethylthiazol-2-yl)-2,5-diphenyltetrazoliumbromide (MTT) were purchased from Sigma-Aldrich (St. Louis, MO, USA).

Male Sprague-Dawley rats (250–300 g) (3 specimens) were acquired from Janvier Labs (France) and maintained under a 12/12 h light/dark cycle (lights on 07:00–19:00 h) at room temperature (22 ± 2°C), with free access to food and water. Rats were housed in group and adapted to these conditions for at least 1 week before experimental manipulation. All experiments were approved by the local authorities (Consejo Superior de Investigaciones Científicas-Universidad Miguel Hernández) and were performed in accordance with Spanish (law 32/2007) and European regulations (EU directive 86/609, EU decree 2001-486).

Stable, Gd-Fe containing, magnetic nanoparticles were synthesized in a two-step process. Initially, paramagnetic Gd^{3+} and superparamagnetic Fe^{3+} centers were combined in the structure of the PB analog $Gd(H_2O)_4[Fe(CN)_6]$ (GF). Here, we controlled the resulting hybrid shape and size by means of varying incorporation of acetic acid, obtaining uniform, monodispersed nanorods of about 100 nm average diameter (GF-1, no acetic acid) or a mixture of monodispersed nanocrosses and nanorods of 230 nm average diameter (GF-2, with acetic acid). Subsequently, isolated GF crystallites were coated with a thin silica layer by polymerization of TMOS at neutral pH in the presence of silicatein α analogues (e.g., TEA), obtaining $Gd(H_2O)_4[Fe(CN)_6]@SiO_2$ particles with the same shape and size than the

pristine PB analog (respectively, GFS-1 and GFS-2). The sequence to obtain the different GFS samples is presented in Fig. 1. For the sake of comparison, we have included the alternative route corresponding to silicate polymerization over GF particles in alkaline medium, to give nanoparticles of $Gd(OH)_3{\cdot}3SiO_2.xH_2O$ composite.[27,28]

Finally, for *in vivo* studies, GFS samples were silanized with 3-aminopropyltriethoxysilane (APTES) and further reacted with PEG_3 precursor to develop a PEG-decorated surface Gd-PB analog (GFS@PEG). An artistic representation of the final GFS-1@PEG material is presented in Fig. 1 inset.

Material synthesis

Synthesis of $Gd(H_2O)_4[Fe(CN)_6]$. $(Et_4N)_3[Fe(CN)_6]$ precursor was prepared according to a known recipe.[30] Briefly, 3.3 g (10 mmol) of $K_3[Fe(CN)_6]$ and 6.3 g (30 mmol) of Et_4NBr were dissolved with 200 mL of methanol in a 500 mL flask connected to a nitrogen line, and stirred at 30° C for 3 days under N_2 atmosphere. The mixture was filtered off and the filtrate was concentrated to approximately 10 mL by rotary evaporation. Resulting solution was stirred with 100 mL of ethyl ether and the yellow precipitate was collected by filtration. The crude was dissolved in 150 mL of refluxing acetonitrile and the solution was allowed to cool, obtaining $(Et_4N)_3[Fe(CN)_6]$. For nanosized PB analog preparation, $Gd(NO_3)_3.6H_2O$ (0.75 g, 1.7 mmol) were dissolved in 50 mL of ethanol:water ($EtOH:H_2O$) mixture (2.5:1 v/v). Then, a solution of the previously synthesized $(Et_4N)_3[Fe(CN)_6]$ (1.0 g, 1.7 mmol, in 25 mL methanol) was added and the mixture was left a day at room temperature. The precipitate was filtered off, washed with ethanol and vacuum dried to yield 62 mg of an orange powder (GF-1). Alternatively, $Gd(NO_3)_3.6H_2O$ (0.75 g, 1.7 mmol) and CH_3COOH

(7.82 g, 235 mmol) were dissolved in 50 mL of EtOH:H_2O (2.5:1 v/v),[30] and the synthesis was completed as described to give 82 mg of GF-2.

Synthesis of $Gd(H_2O)_4[Fe(CN)_6]@SiO_2$. Silica coated GF samples were prepared by adding CPTMS (417 µL, 2.19 mmol) to GF suspension (441 mg GF, 1 mmol, in 221 mL of EtOH:H_2O mixture, 2.5:1 v/v) with vigorous magnetic stirring, to make vitreophilic GF surface. After 30 minutes, 1.1 mL of TMOS (7.29 mmol) and 44 µL (0.31 mmol) of TEA were slowly added, to adjust pH 7. The resulting dispersion was allowed to stir for 24 h at room temperature. Afterwards, a second equal addition of TMOS was carried out and the mixture was stirred for another 24 h. Finally, non-reacted silicate ions were thoroughly removed by subsequent centrifugation (484 *g*, 2 h), and the obtained orange solid was washed five times with EtOH:H_2O mixture (2.5:1 v/v), and further freeze dried (-55 ºC, 16 h).

Synthesis of $Gd(H_2O)_4[Fe(CN)_6]@SiO_2@PEG_3$. PEGylation over GFS material was done by using a method previously described by our group.[31] 331 mg of GFS was dried at 80 ºC and vacuum (8 torr) for 24 h. Then, 13.30 mL of anhydrous toluene was added and the mixture was heated to reflux. 646 µL (2.78 mmol) of 3-aminopropyltriethoxysilane (APTES) was added and the mixture was stirred for 3 h. The obtained product was filtered off, washed with toluene and methanol and freeze-dried (-55 ºC, 16h). Subsequenty, 285 mg of the silanized material were suspended in 28.5 mL of anhydrous dichlorometane, and 356 µL of diisopropyl amine were injected under nitrogen atmosphere. Afterwards, 221 mg of PEG_3 were added, and the mixture was stirred overnight at room temperature. The solvent was removed under reduced pressure and the nanoparticles, suspended in 100 mL of ethanol

with stirring. This suspension was filtered off and washed with ethanol (300 mL). Finally, the material was freeze-dried (-55 ºC, 16 h).

Material characterization

Powder X-ray diffraction (XRD) patterns were collected in a Philips X'Pert diffractometer equipped with a graphite monochromator, operating at 40 kV and 45 mA and using nickel-filtered Cu Kα radiation λ = 0.1542 nm). Liquid nitrogen adsorption isotherms of 200 mg of sample were measured in a Micromeritics Flowsorb apparatus. Surface area calculations were done by the BET method. Infrared spectra were recorded at room temperature in the 400−3900 cm^{-1} region with a Nicolet 205xB spectrophotometer, equipped with a Data Station, at a spectral resolution of 1 cm^{-1} and accumulations of 128 scans. Samples for transmission electron microscopy (TEM) were ultrasonically dispersed in a mixture EtOH:H_2O (2.5:1 v/v) and transferred to carbon coated copper grids. TEM micrographs were collected in a JEOL JEM 2100F microscope operating at 200 kV. The quantitative EDS analysis was performed in an INCA Energy TEM 250 system from Oxford Instruments, working with a SDD X-MAX 80 detector. Field-emission scanning electron microscopy (FESEM) micrographs were collected in a ZEISS Ultra 55 microscope operating at 2 kV, with a 2×10^{-9} A beam current and 2.5 mm as the working distance. Particle size and Z-Potential measurements were conducted by diffuse light scattering (DLS) in a Zetasizer Nano ZS (Malvern Instruments Ltd., Worcestershire, UK). Dried material was re-suspended at a concentration of 5 μg/mL in deionized water or phosphate buffer saline (PBS) and measurements were performed at 25 ºC. The mean hydrodynamic diameter was determined by cumulant analysis. Organic and water content in as-prepared

material were calculated from elemental analysis (FISONS, EA 1108 CHNS-O) and thermogravimetric (TGA) measurements (Mettler-Toledo TGA/SDTA851$_e$).

GFS@PEG material stability in isotonic medium was monitored by dialysis solution assay in aqueous glucose (5.0 wt%) and simulated body fluid (SBF).[32] 11 mg of the corresponding material were introduced in a dialysis tubing with 2 mL of glucose solution. Then, filled dialysis tubing was inserted in a glass bottle with 50 mL of fresh solution, and the system was stirred at 90 rpm and 37°C in a thermostatic bath for seven days, changing the bottle solution by fresh solution at the corresponding sample time. Subsequently, leached Fe^{3+} concentration was analyzed by inducted couple plasma (ICP, Varian 715-ES) or inducted couple plasma mass spectrometry (Varian 820-MS).

Relaxivity measurements and *in vitro* MRI

Relaxivity determinations were carried out in a clinical Phillips 3 T MRI unit (Achieva 3 T X-Series; Philips Healthcare, The Netherlands) using a 8-channel phased array head coil, and in a Bruker 9.4 T spectrometer (AV400) working with a 90º pulse of 5 µs and a recycle delay of 5 s. T_1 and T_2 relaxation times were measured using inversion recovery and cpmg pulse sequences respectively. For the *in vitro* MRI study (Philips Achieva 3 T X-Series), the phantom was scanned with single slice in coronal orientation obtaining transversal view of all tubes filled with variable CA concentration in a xantham gum solution (0.1 wt%). Geometric parameters remain equivalent between T_2 and T_1 estimation sequence (Field of View –FOV- 220x220 mm^2, slice thickness 5 mm and 1.0 x 1.0 mm^2 in plane resolution) sharing the same spatial localization. Multi-echo spin echo sequence was used to estimate T_2 values acquiring 32 echoes ranging from 14 to 231 ms (ΔTE=7 ms) with a Repetition

Time (TR) of 2000 ms. T_1 values of each tube were estimated using a look-locker inversion recovery acquisition with 107 inversion times ranging from 6.51-5306.51 ms, with an inversion time interval of 50 ms. A new inversion pulse was applied every 6 s to avoid signal saturation due to extremely close inversion pulses. To reduce the influence of readout excitation pulse in the final T_1 values, an excitation flip angle of 5º was applied during the TFE shot.[33] T_2 maps were generated by a pixel by pixel nonlinear fitting of the signal acquired at every Echo Time (TE) to a mono-exponential model. T_1 maps were generated by pixel by pixel nonlinear fitting of the signal acquired at every inversion time to the signal model of ref. 30. Quantitative values were obtained in aqueous xanthan gum (0.1 %) nanoparticle suspensions. For each tube, a circular ROI was placed manually over T_2 and T_1 maps avoiding the border. For each ROI, mean and standard deviation were computed for further comparison.

The resulting T_1 and T_1 values were averaged and plotted as $1/T_i$ (s^{-1}) where i =1, 2 against the experimentally calculated metal concentration (mM), [Gd^{3+}] for T_1 and [Fe^{3+}] for T_2. The slopes of these graphs provided the specific relaxivities r_1 and r_2.

Cytotoxicity assay

The different cell lines were cultured in 96-well cell culture plates with the seeding densities shown below in a final medium volume of 200 µL/mL: HeLa 10000 cells/well; 3T3 and 42-MGBA 50000 cells/well and SH-SY5Y 100000 cells/well. HeLa cells were grown in MEM (Earle's), 3T3 cell line in DMEM, 42-MGBA cell line in MEM (Earle's) and RPMI 1640 (1:1), and SH-SY5Y cell line was cultured in a DMEM and Ham (F12) Nut MIX (1:1). Cell mediums were supplemented with 10% FBS and Pen-Strep 1:100 (v/v). The plates were

cultured 24 h at 37 ºC and 5% CO_2 injection in air. After 24 h cells were treated with variable concentrations of the CA (0.25-100 µg/mL in RPMI medium). Culture medium was used as negative control. Cells were incubated in 5% CO_2 at 37ºC for 24 h.

Cell viability was measured using the 3-(4,5-dimethylthiazol-2-yl-diphenyltetrazolium bromide) (MTT) assay. 200 µL/well of MTT/PBS (1 mg/mL) were added and the plates were incubated at 37 ºC for 3 h. Formazan crystals were dissolved with 100 µL DMSO and then absorbance at 595 nm was measured with a 1681130 iMark™ Microplate Reader. Absorbance values were normalized with respect to the controls and expressed in percentage using the next equation:

$$Relative\ cell\ viability\ = \frac{OD_{595\ TEST\ SAMPLE}}{OD_{595\ CONTROL}} * 100$$

Data statistical analysis was performed applying arithmetic means and error bars of statistical error means (SEM) using Matlab (MathWorks). IC50 calculation survival data were calculated by nonlinear regression sigmoidal dose–response (variable slope) curve-fitting using Prism 6.0 software (GraphPad, San Diego, CA). At least three independent experiments were performed for every sample, and each experiment was carried out by triplicate.

***In vivo* MRI study**

Experiments were carried out in a horizontal Bruker 7 T scanner with a 30 cm diameter bore (Biospec 70/30v, Bruker Medical, Ettlingen, Germany). The system had a 675 mT/m actively shielded gradient coil (Bruker, BGA 12-S) of 11.4 cm inner diameter. A ^{1}H rat body receive-transmitter resonator (Bruker BioSpin MRI GmbH, Germany) was employed. Data were acquired with a Hewlett-Packard console running Paravision software (Bruker

Medical GmbH, Ettlingen, Germany) operating on a Linux platform. Rats were anesthetized in an induction chamber with 3-4% isofluorane in medical air (0.8-1 L/min) and maintained with 1-2 % isofluorane (IsoFlo) during the MRI experiment. Anesthetized animals were taped down in a custom-made animal holder to minimize breathing-related movement artifacts. Body temperature was kept at 37 ºC using water blanket and animals were monitored using a MRI compatible temperature control unit (MultiSens Signal conditioner, OpSens, Quebec, Canada). Breathing rate was also measured using a customized device.

Studies were performed by injecting 1 mL of the CA suspension (5 mg mL^{-1}) into the catheterized tail vein as a single bolus (0.05 mmol Gd/kg body weight, 0.05 mmol Fe/kg body weight). T_2 weighted anatomical images to position the animal were collected in the three orthogonal orientations using a rapid acquisition relaxation enhanced sequence (RARE), applying the following parameters: FOV 40 x 40 mm, 15 slices, slice thickness 1 mm, matrix 256 x 256, effective TE (TE_{eff}) 56 ms, TR 2 s, 1 average and a total acquisition time of 64s.[34,35] Two types of images were used to assess the effect of CA in the SI in T_1 and T_2 weighted images. For the former, FLASH images were acquired with the following parameters: 25 slices, 1.5 mm slice thickness, TR 197 ms; TE 2.7 ms; FOV 6.0x5.0 cm; matrix 128x108; 4 averages; total acquisition time 90 s. Three images were acquired before CA administration (baseline) and 20 after it. For the T_2 weighted images, RARE sequence was used with the same geometry than T_1 weighted images and the following parameters: TR 2800 ms; TE 48 ms; FOV 6.0x5.0 cm; Mtx 256x214; 8 averages; total acquisition time 600 s. One of these images was acquired at the beginning (baseline) and one at the end of the experiment. Data were analyzed with Image J (W. S. Rasband, U.S. National Institutes of Health, Bethesda, MD, http://rsb.info.nih.gov/ij/, 19972005).

Pathological investigation after MRI

After *in vivo* MRI experiments, rats were euthanized and samples of lung, heart, liver and spleen were collected for subsequent histological analysis. These organs were immersed in 4% parafolmaldehyde for 24-48 h. Tissues were then included in paraffin and cut with a microtome 5-7 μm thickness slices. Finally, these sections were deparaffinized and stained with Hematoxylin/Eosin staining. Histology images were taken using Olympus AX70 microscope.

Results and discussion

Synthesis and characterization of stable Gd-Fe based magnetic nanoparticles

The strategy to obtain GFS hybrids is comparatively depicted in Fig. 1. As commented, in this synthesis scheme there are two crucial points to be accomplished: i) the role of acetic acid in shape and size distribution; and ii) an accurate pH control during silicate polymerization. $Gd(H_2O)_4[Fe(CN)_6]$ nanocrystals with well-defined morphology can be obtained with dual shape (e.g., crosses and rods, with an average diameter over 260 nm, and shape ratio of about 1:2, as determined by TEM) or like single nanorods (over 95 nm average diameter) (Table S1 in Supplementary Information). A possible mechanism for nanocrosses formation indicates that Et_4N^+ works as a cationic surfactant, cooperating in the synthesis with acetic acid to function as a soft template that forces Fe-CN-Gd crystals to assemble in the cross morphology.[36] Actually, in the absence of carboxylic acid, only small and uniform rods grow.

On the other hand, the obtained GF compound is partially soluble in water, but is stable in EtOH:H_2O mixture (2.5:1 v/v). However, if the silica coating process is carried out with

sodium silicate (pH>8.5), an ion exchange reaction takes place, resulting in complete GF dissolution and concurrent $Gd(OH_3)$ precipitation. By overlapping this process with

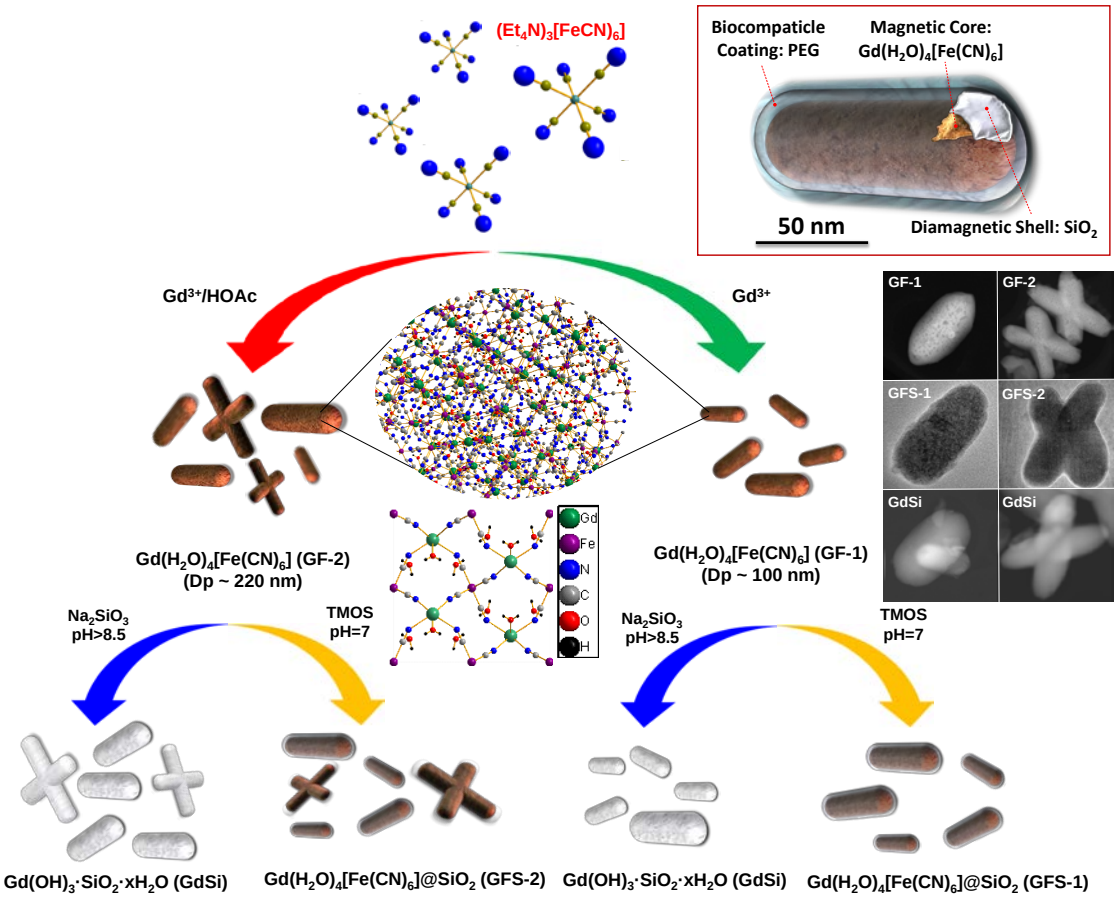

Fig. 1. Sequence of the stepwise biomimetic strategy followed to obtain GFS materials and alternative synthetic routes. The inset shows an artistic representation of final GFS-1@PEG nanoparticles.

silicate hydrolysis and condensation, a simultaneous and stoichiometric condensation of $Gd(OH)_3$ and SiO_2 takes place, yielding the nanocomposite $Gd(OH)_3{\cdot}3SiO_2{\cdot}xH_2O$ (Fig. 1).[27,28] Conversely, under neutral pH obtained by a biomimetic synthetic strategy that takes advantage of silicatein α functional analogues as TEA, silica wall grows homogeneously over CPTMS-functionalized GF nanoparticles, to give GFS material. No significant GF compound solution is observed during the coating process (iron leaching quickly stains the

medium in yellow), resulting in $Gd(H_2O)_4[Fe(CN)_6]@SiO_2$ particles with same morphology and similar size distribution than pre-formed PB analog crystals. At this point, a slight increase in particle average diameter is observed in the case of GFS-1 sample small rods. However, GFS-2 suffers some particle size reduction after silica coating, which may be attributed to partial destruction of some bigger nanocrosses during the treatment (as confirmed by the drop in crosses/rods ratio, see Table S1 in Supplementary Information).

These silica protected nanoparticles are expected to be stable in aqueous medium, in agreement with a Z-Potential lower than -10 mV (Table S1 in Supplementary Information). Nevertheless, DLS hydrodynamic diameter of GFS samples in water (GFS-1=124.7±81.9, GFS-2=343.7±154.1) is significantly larger than TEM measurements (GFS-1=106.7±33.5, GFS-2=230.3±35.5) (Fig. S1 in Supplementary Information), which is due to some particle aggregation in water, with the polydispersity index (PdI) varying from 0.2 to 0.4 (Table S1). In addition, the stability in PBS is clearly compromised by the high ionic strength of this medium, leading to very unstable suspensions were aggregation takes place in large extension (PdI=1, Table S1). This is notably overcome by PEGylating the samples (0.05-0.06 mmol PEG_3/g, as determined by TGA). Obtained DLS hydrodynamic diameters for GFS@PEG samples (GFS-1@PEG=111.4±62.7, GFS-2@PEG=228.9±79.3) are very similar to real size determined by TEM (Fig. S1), and PdI values are clearly lower than GFS suspensions (Table S1). Moreover, PEGylation significantly reduces aggregation in PBS (although does not fully suppress it), allowing to prepare reasonably stable suspensions of these nanoparticles. Besides, PEGylation contributes to minimize the immunogenic reaction under *iv* administration.[31]

Powder X-Ray reports reveal that GF structure is fully retained after the silica coating process (Fig. S2 in Supplementary Information). Also, the final PEGylation step does not involve any significant change in the XRD pattern. $Gd(H_2O)_4[Fe(CN)_6]$ crystallizes in the orthorhombic system with C_{mcm} space group and cell parameter of a = 7.4016(3) Å, b = 12.78813(14) Å, and c = 13.5980(12) Å. In addition, it is remarkable that the nanosized material XRD patterns are fully comparable to that of the bulk compound.[23]

Electronic microscopy study (Fig. 2) confirms the formation of monodispersed nanoparticles with a thin (6-10 nm width), continuous and homogenous silica shell over $Gd(H_2O)_4[Fe(CN)_6]$ core. EDS analysis is consistent with the expected PB analog stoichiometry (Gd:Fe atomic ratio = 1), although there are small deviations that we attribute to the accuracy of the analytical technique over single nanoparticles. Moreover, the spatial distribution of Si, Gd and Fe in isolated particles can be observed by elemental mapping (Fig. 2i-l), which illustrates the homogeneous distribution of Gd and Fe in the core, as well as the solely presence of Si at the shell. This can be clearly stated in Fig. 2d, which shows EDS line scans corresponding to the different elements present inwards (Gd, Fe) and outwards (Si) . In addition, no change is observed in the closely packed structure of the PB analog and estimation of interplanar distance over the [112] plane by TEM matches reasonably well the theoretical calculation from Bragg's law (Fig. 2g-h).

FTIR reports display two peaks at 2140 and 2150 cm^{-1} corresponding to stretching vibration of Fe-CN-Gd bond, and an additional *st* vibration at 2070 cm^{-1} (Fig. S3 in Supplementary Information). The low energy signal is originated from ferrocyanide $[Fe(CN)_6]^{4-}$, which is probably generated by ferricyanide $[Fe(CN)_6]^{3-}$ reduction by alcohol during the synthesis.[36]

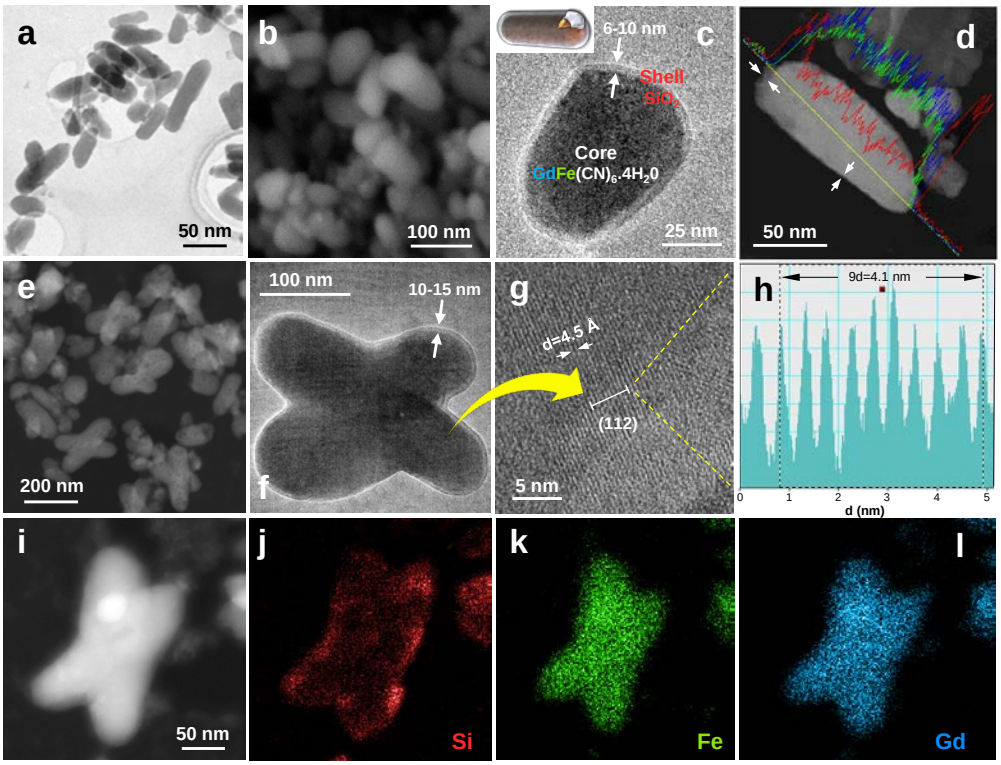

Fig. 2. Electron microscopy study of as-synthesized GFS materials. (a,b): GFS-1 sample general images by TEM (a) and FESEM (b). (c) High resolution TEM image of a GFS-1 nanorod showing its core-shell nature. The inset shows an artistic representation. (d) EDS line scans of a GFS-1 nanorod depict the changes in composition from particle outer surface to the inner core. (e) GFS-2 sample general image by STEM. (f) High resolution TEM image of GFS-2 nanocross showing its core-shell nature. A magnification of this picture in (g) allows to observe the PB analogue closely packed structure at the [112] plane. Also, interplanar distance calculation by TEM over 10 sheets (h) matches quiet good the theoretical calculation from the Bragg's law. (i-l) EDS elemental mapping pictures of a GFS-2 nanocross.

Small peaks in the range 1610-1630 cm^{-1} are assigned to δ(H-O-H) vibration.[37] Conversely, a sharp ν(H-O) signal is present at 3610 cm^{-1} and an intense broad band ν(H-O-H) is observed in the range 3000-3550 cm^{-1}.[37,38] After endowing the GF particles with the silica coating, a new broad signal centered at 1085 cm^{-1} appears, corresponding to ν(Si-O-Si) vibration. In addition, PEGylated samples show small peaks in the range 2850-2950 cm^{-1}, which are due to ν(C-H) of methylene groups.

The silica coating reveals itself crucial for the stability of these hybrids in physiological fluids. GF material is partially soluble in water and physiological fluids, leaching significant quantities of metal cations over a short period. To study this we dispersed GFS-1@PEG at 37 ºC in isotonic glucose 5 wt% medium or in SBF and monitored the leached metal concentration by ICP/ICP-MS (Fig. S4 in Supplementary Information). Unfortunately, in these testing conditions, most of the released Gd^{3+} is quickly precipitated as $Gd(OH)_3 \cdot xH_2O$, remaining in the dialysis bag as a white powder, so the obtained Gd^{3+} concentration in dialysis samples is very low and can't be used as a pattern of metal leaching (total Gd^{3+}quantity measured in solution by ICP-MS was lower than 0.5 %). In this context, Fig. S4 in Supplementary Information shows only Fe^{3+} leaching in glucose 5% solution (as determined by ICP) and in SBF (as determined by ICP-MS). We observed negligible metal leaching in the first 4 h (<1 %) and about 5-11 % at 24 h, which makes this material suitable for *in vivo* MRI (image acquisition takes place no longer than 1-2 hours after *iv* administration). Furthermore, even after 7 days, the concentration of leached metals was lower than 25% in both mediums. This is also important, as it implies very slow particle degradation, which should allow almost complete particle elimination by renal and biliary routes before reaching toxicity.[39]

It is noticeable that the coating process is determinant not only to prevent PB analog solution in aqueous medium, but also to increase hybrid surface area, as the highly packed Gd-Fe structure is difficult to functionalize with organic ligands. In this sense, the adsorption pattern obtained from the nitrogen isotherms over silica covered samples correspond to amorphous, non-porous materials, with an external surface area over 60 $m^2\ g^{-1}$ (Table S1

and Fig. S5 in Supplementary Information). This is enough for subsequent incorporation of different functionalities, as therapeutic agents, targeting compounds and/or PEG molecules.

Relaxivity measurements and *in vitro* MRI

The efficacy of GFS material as T_1- and T_2 MRI CA was evaluated by measuring the longitudinal (r_1) and transversal (r_2) nuclear magnetic relaxation rates of water proton in aqueous suspensions at room temperature and magnetic field of 3 T and 9.4 T. Stable colloids were prepared in aqueous xantham gum (0.1 wt%) solution with M^{3+} concentration in the range 0-1.00 mM (Gd^{3+} for T_1, Fe^{3+} for T_2). Relaxivity values were determined by using the following expression:[40]

$$\frac{1}{T_{i(w)}} = \frac{1}{T_{i(0)}} + r_i C$$

Where i = 1 or 2 values, respectively, for longitudinal or transversal-weighted effect of CA. $1/T_i(w)$ is the global relaxation rate constant of bulk water molecules, $T_i(0)$ is the water relaxation time without CA, and C is the paramagnetic ion concentration. r_1 and r_2 values were determined, respectively, from the slopes of $1/T_1$ (s^{-1}) and $1/T_2$ (s^{-1}) versus M^{3+} concentration (Table 1 and Fig. S6 in Supplementary Information). For the sake of comparison, same measurements were carried out with commercial CA gadopentetate dihydrogen salt (Gd-DPTA, Sigma-Aldrich).

GFS-1 and GFS-2 show high r_1 and r_2 values at high magnetic field (9.4 T), of about 1 order superior to that of Gd-DPTA (Table 1).

Table 1 Longitudinal and transverse relaxivities of hybrid GFS materials.

Sample	r_1 (s^{-1} mM^{-1})	r_2 (s^{-1} mM^{-1})	r_2/r_1
B_0=9.4 (T)			
Gd-DTPA	4.4	4.6	1.04
GFS-1	13.1	66.6	5.1
GFS-2	11.7	58.6	5.0
GFS-1@PEG	20.8	69.9	3.4
GFS-2@PEG	16.7	59.6	3.6
B_0=3.0(T)			
Gd-DTPA	3.8	3.0	0.8
GFS-1@PEG	27.0	35.1	1.3

A dramatic T_2 reduction is expected with regards to the commercial chelate due to the presence of a huge population of Fe^{3+} centers in GFS samples. However, the increased r_1 value compared to mononuclear species of Gd^{3+} is mostly due to the spin order of Gd^{3+} runs parallel to the local magnetic field induced by the superparamagnetic Fe^{3+} center domains under an external magnetic field.[17] Also, the partial contribution of T_1 shortening by Fe^{3+} sites may enhance T_1 contrast effect. This synergistic effect is possible by the extremely dense Gd^{3+} and Fe^{3+} ion packaging at the same crystalline structure, which are connected via cyano-bridge bonds.[23] Actually, a perspective view of the network topology of GF structure at Fig. 3 shows two different Gd-Fe non-bonding distances, estimated as 5.509 and 5.352 Å. A similar synergistic effect has been observed when embedding Gd oxide crystallites into iron nanoparticles,[21,26] and also in other similar materials.[41]

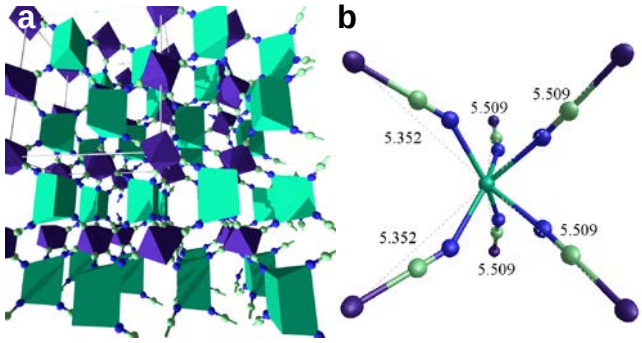

Fig. 3. (a) Perspective view of the network topology of $Gd(H_2O)_4[Fe(CN)_6]$, where water molecules have been removed. Gd, is at the center of the green triangular prisms; and Fe is at the center of the octahedra. When water is considered, two water molecules coordinate to each Gd atom giving a square anti-prism coordination for Gd. (b) Perspective view of the structure and coordination of a Gd atom in the $Gd(H_2O)_4[Fe(CN)_6]$ structure. Two water molecules have been omitted for clarity. Two different non-bonding distances Gd-Fe appear, 5.509 Å (4) and 5.352 Å (2).

At this point, we are aware of the fact that the external silica coating could be an issue over the magnetic properties of GFS samples, mostly over longitudinal relaxation. According to Solomon-Bloembergen-Morgan theory, T_1 shortening is related to directly bound water molecule interactions over magnetic centers, corresponding to the inner sphere relaxation mechanism.[7,8] This interaction is hindered in nanoparticles fully covered with an homogeneous and non-porous silica shell. However, contrast agents can display relaxivity even when there is no water in the inner coordination sphere, and in this case the relaxivity comes from outer sphere contributions, where water molecules hydrogen bonded to silica surface are relaxed *via* dipolar mechanisms.[42]

Moreover, r_1 gain is clearly higher for PEGylated samples (of about 60% for GFS-1 and 45% for GFS-2, Table 1). As T_1 shortening is mainly related to the chemical exchange of protons with M^{3+} centers at the water sphere regime, it should improve when particle external surface area increases.[7,8,42] In this context, PEGylation may stabilize the magnetic

colloid by reducing particle aggregation and hydrodynamic diameter (Table S1 and Fig. S1 at the Supplementary Information), which promotes surface interaction with water molecules. Here, other authors have reported the strong effect of PEGylation over water exchange and water molecule access to Gd^{3+} centers, and its influence over longitudinal relaxivity.[43] Conversely, PEGylation shows a modest effect over transversal relaxivity (a very short increase of 2-4% at B_0= 9.4 T, Table 1), as r_2 is little dependent on metal ion hydration, mean residence time of the water molecule in the first coordination sphere, and the tumbling rate of the species.

In the same line, the modest r_1 increase in GFS-1 and GFS-1@PEG hybrids with regards, respectively, to GFS-2 and GFS-2@PEG samples is assumed as consequence of the smaller particle size.[44] Such effect is even stronger at lower magnetic field intensity (3 T), with the r_2/r_1 ratio getting close to 1 (GFS-1@PEG sample, Table 1). This, together with a relatively high r_2 value prompt the use of GFS material as T_1-T_2 dual-modal MRI CA.

To further check this capability, phantom MRI images with GFS-1@PEG sample (Fig. 4) were collected. For the purpose of comparison, two regular T_1-agents, commercial Gd-DPTA chelate (r_1 = 4.1 mM^{-1} s^{-1}, r_2 = 3.3 mM^{-1} s^{-1}) and Gd-Si oxide nanoparticles (GdSi, r_1 = 5.6 mM^{-1} s^{-1}, r_2 = 8.2 mM^{-1} s^{-1}),[28] were also tested. The phantoms were scanned with a single slice in coronal orientation. Fig. 4a shows the T_1-weighted images of the different materials at variable CA concentration based on Gd^{3+} content. Both GdSi and Gd-DPTA display a similar signal enhancement depending on concentration. However, GFS-1@PEG presents a much stronger contrast effect, due to the described synergistic effect between Gd^{3+} and Fe^{3+} magnetic centers. Such differences are stressed in a T_1-weighted image of a single slice in transversal orientation obtained at 1 mM of Gd^{3+} (Fig. 4b). In addition, Fig.

4c presents the T_2-weighted images corresponding to these samples at variable M^{3+} concentration (Gd^{3+} for GdSi and Gd-DTPA, Fe^{3+} for GFS-1@PEG). As expected, the GFS hybrid exhibits superior dark contrast performance due to the presence of Fe^{3+} superparamagnetic centers.

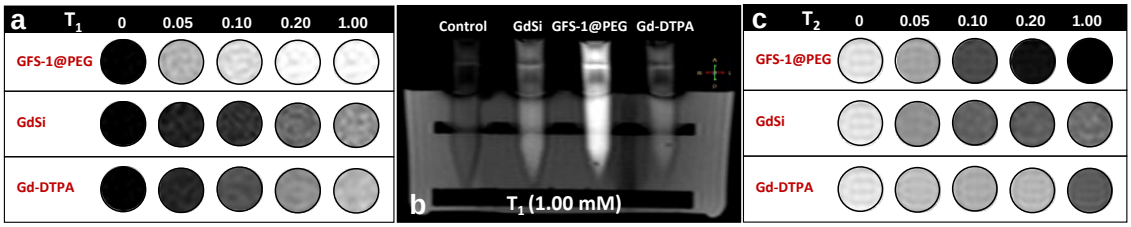

Fig. 4. Phantom MRI images of GFS-1 sample and two regular T_1-agents, commercial Gd-DTPA and Gd-Si oxide nanoparticles (GdSi).[28] (a) T_1-weighted MRI coronal slices at magnetic field of 3 T and echo time of 2 ms over varying Gd^{3+} concentration. (b) T_1-weighted MRI transversal slice at magnetic field of 3 T and echo time of 2 ms over Gd^{3+}=1 mM. (c) T_2-weighted MRI slices at magnetic field of 3 T and echo time of 203 ms over varying M^{3+} concentration (Gd^{3+} for GdSi and Gd-DTPA, Fe^{3+} for GFS-1).

Cytotoxicity study

To validate GFS nanoparticle potential performance in a biological environment, cell viability was assessed 24 h after incubation with the GFS-1 sample by determination of 3-(4,5-dimethylthiazol-2-yl)-2,5-diphenyltetrazolium bromide (MTT) conversion to its formazan form, by following standard procedures. We used healthy fibroblasts (3T3 cell line) and three different cancer cell lines (HeLa cells, 42-MG-BA glioblastoma multiforme cells and SH-SY5Y neuroblastoma cells) at a range of concentrations (0.25-100 μg mL^{-1}). Results (Fig. S7 in Supplementary Information) indicate that even at the highest particle loading, relative cell viability was above 70%. Actually, despite MTT testing inherent limitations for accurate cell viability determination, these results correspond to an acceptable biocompatibility profile.[45]

In vivo dual T_1 and T_2-weighted MRI

Direct *iv* administration of GFS-1 nanoparticles is precluded due to the immediate and strong reaction with serum proteins, which results in protein corona formation. This promotes subsequent interaction with cell elements of the reticuloendothelial system, and rapid particle clearance from blood, which are accumulated mostly in liver, spleen and lungs.[46] In order to minimize this non-specific immunogenic process, GFS-1 nanorods were modified with a short PEG chain, according to a known recipe,[31] to give GFS-1@PEG. This way, nanoparticles are expected to prolong their blood circulation time, finally being eliminated mainly by renal (urine) and hepatic (biliary) routes.[38,47] Subsequently, 1 mL of a 5 mg mL^{-1} GFS-1@PEG stable colloid in glucose 5% was perfused into the catheterized tail vein of healthy male Sprague-Dawley rats as a bolus (~0.05 mmol Gd kg^{-1} and 0.05 mmol Fe kg^{-1}). After 30 min, T_1- and T_2-weighted images were acquired for 1 h by using a 7 T horizontal scanner. Previously to CA administration images, baseline images were processed.

Fig. 5 shows coronal T_1- and T_2-weighted MRI before (baseline) and after CA. For the sake of clarity, the different regions of interest (ROIs) presenting the most significant signal to noise ratio (SNR) changes have been manually labeled over pre-injection images. SNR changes are compiled in Table 2. T_1-weighted images show clear positive signal enhancement in liver (ΔSNR = 17.3 % relative to baseline, Fig. 5a,a') and kidneys (ΔSNR = 6.4 %, Fig. 5c,c'). This is not surprising as these organs receive most of the blood stream, which favors highly promoted particle accumulation. Despite its large size and lobular shape, liver presented mostly uniform changes in SI, which corresponds to a homogeneous nanoparticle biodistribution over the entire organ. In addition, T_2-weighted images present

strong negative contrast for liver (ΔSNR = 27.8%, Fig. 5b,b'), gallbladder (ΔSNR = 78.0%, Fig. 5b,b') and kidneys (ΔSNR = 51.7%, Fig. 5d,d'). In all cases, the contrast enhancement remains fully stable during the whole acquisition time (1 h), although a significant extension of acquisition period should be feasible.

Table 2 Magnitude of the normalized changes in the signal to noise ratio (SNR) of T_1- and T_2 weighted images after *iv* administration of GFS-1@PEG in a Sprague-Dawley rat (0.05 mmol Gd Kg^{-1} and 0.05 mmol Fe Kg^{-1}). Values correspond to mean ΔSNR averaged over 15 min after the injection.

Region of Interest	**ΔSNR (%)**
T1-weighted images	
Liver	17.3
Gallbladder	0.1
Paraspinous muscle	3.0
Kidney	6.4
T2-weighted images	
Liver	27.8
Gallbladder	78.0
Paraspinous muscle	6.3
Kidney	51.7

Furthermore, no structural or cellular abnormalities were detected in lung, heart, spleen and liver slices of treated animals. Fig. 6 shows some representative examples of histological sections in a CA administered rat (Fig. 6a-h) and the same histological plates for a non-administered specimen (control, Fig. 6i-p).

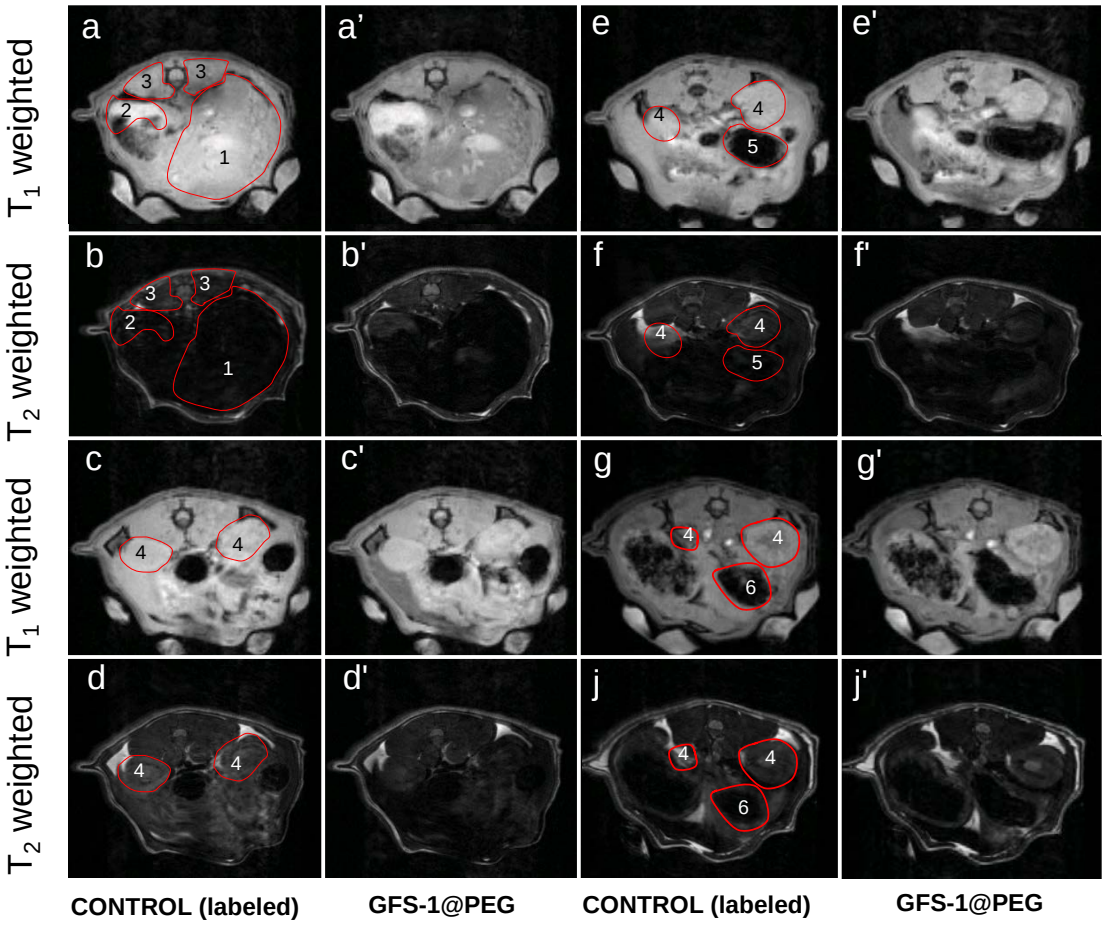

Fig. 5. *In vivo* coronal T_1- and T_2-weighted images acquired from a male Sprague-Dawley rat at 7 T magnetic field. (a-j) Control (baseline) with no MNP administration. The following ROIs have been manually labeled (red lines): 1-liver; 2-gallblader; 3-paraspinous muscle; 4-kidney; 5-stomach; 6-pancreas. (a'-j') Acquisition 30 min after GFS-1@PEG nanorod injection (0.05 mmol Gd^{3+} kg^{-1}, 0.05 mmol Fe^{3+} kg^{-1}).

Liver histology (Fig. 6a,b and 6i,j**)** does not display haemorrhages in hepatic vein and arteries, neither shows damage or abnormalities in the liver lobules cells or structure. No abnormities were seen in spleen histology (Fig. 6c,d and 6k,l**)** in the white and the red pulp. Lymph nodes structure was normal and no signs of haemorrhages or high immune system activity were observed.

Also, heart myocardium histology was not been affected by the CA (Fig. 6e,f and 6m,n). Regarding pericardium and endocardium, both structures were kept intact after agent contrast administration (images not shown). Finally, lung histological slices (Fig. 6g,h and 6o,p) showed no pulmonary failure signs and intact alveolar and bronchial structures.

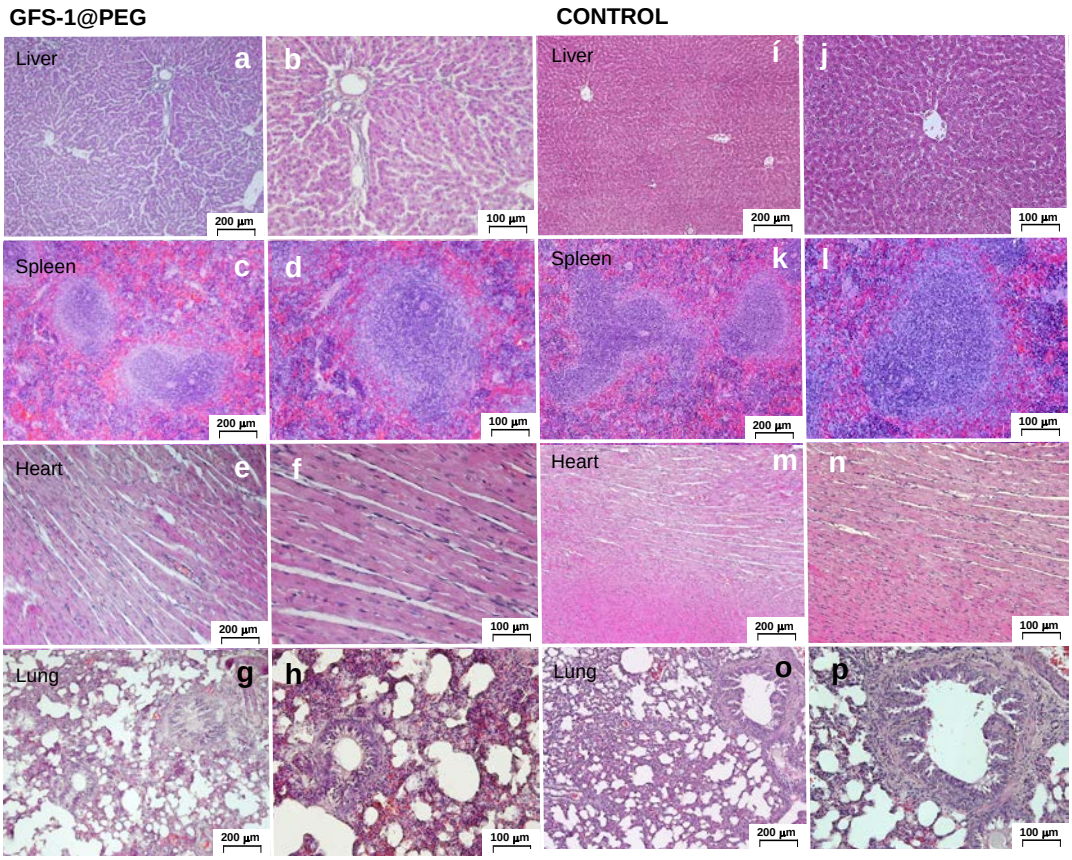

Fig. 6. (a-h) Hematoxylin/eosin staining of histological slices after administration (single bolus) of GFS-1@PEG (0.05 mmol Gd^{3+} kg^{-1}, 0.05 mmol Fe^{3+} kg^{-1}). (i-p) Same histological slices in a control specimen.

Overall, these findings indicate that PEGylated GFS material is highly biocompatible dual CAs able to provide both positive T_1 and negative T_2 contrast enhancement in MR imaging. This is a consequence of the GFS improved characteristics as MRI CA, presenting consistent stability in biological fluids and high longitudinal and transversal relaxivity

values due to the synergistic effect between Gd^{3+} and Fe^{3+} centers in a closely packed crystalline structure.

Conclusions

The incorporation of T_1 and T_2 active moieties in a CA for dual-modal MRI provides complementary information that can help to improve the safety of diagnosis. In this sense, we have developed a novel hybrid material with high performance as MRI CA by optimizing the synthesis of $Gd(H_2O)_4[Fe(CN)_6]$ magnetic nanoparticles with controlled size and morphology, covering them with a thin diamagnetic silica layer by following a biomimetic strategy for silicate hydrolysis and polymerization at neutral pH. The obtained system shows long-term stability in physiological fluids because of the protecting non-porous outer shell. This material presents longitudinal relaxivity values over one order superior to regular T_1 Gd^{3+} based systems and much stronger positive contrast in *in vitro* and *in vivo* MR images, due to the synergistic effect between Gd^{3+} and Fe^{3+} magnetic centers closely connected *via* cyano-bridge bonds in a highly packed crystalline structure. In addition, the GFS hybrid exhibits transversal relaxivity data comparable to that of iron oxide nanoparticles, which provides strong dark contrast performance in *in vitro* and *in vivo* MRI. The lack of cytotoxicity checked in different cell lines and the absence of histological damage observed in the main organs of tested animals indicate a good biosafety profile, stressing the potential of this CA in clinical applications. With regards other proposed T_1-T_2 dual mode CAs, these nanoparticles present very homogeneous composition and constant Gd:Fe atomic ratio, providing reproducible quality in MRI signal.

Conflicts of interest

There are no conflicts of interest to declare.

Acknowledgements

Financial support of the Spanish Ministry of Economy and Competitiveness (projects TEC2016-80976-R and SEV-2016-0683) is gratefully acknowledged. Dr. E.M. Rivero thanks the Cursol Foundation for a post-doctoral scholarship. A.C.G. also thanks the La Caixa Foundation for a Ph.D. scholarship. We fully appreciate the assistance of the Electron Microscopy Service of the UPV and INSCANNER S.L.

References

1 P. J. Bolan, M. T. Nelson, D. Yee and M. Garwood, *Breast Cancer Res.*, 2005, **7**, 149.

2 R. E. Mitchell, M. H. Katz, J. M. McKiernan and M. C. Benson, *Nat. Rev. Urol.*, 2005, **2**, 356.

3 M. Colombo, S. Carregal-Romero, M. F. Casula, L. Gutierrez, M. P. Morales, I. B. Bohm, J. T. Heverhagen, D. Prosperi and W. J. Parak, *Chem. Soc. Rev.*, 2012, **41**, 4306.

4 R. Zakaria, K. Das, M. Bhojak, M. Radon, C. Walker and M. D. Jenkinson, *Cancer Imaging*, 2014, **14**, 8.

5 P. Mi, D. Kokuryo, H. Cabral, H. Wu, Y. Terada, T. Saga, I. Aoki, N. Nishiyama and K. Kataoka, *Nature Nanotechnol.*, 2016, **11**, 724.

6 W. Cheng, Y. Ping, Y. Zhang, K. H. Chuang and Y. Liu, *J. Healthc. Eng.*, 2013, **4**, 23.

7 R. B. Lauffer, *Chem. Rev.*, 1987, **87**, 901.

8 P. Caravan, J. J. Ellison, T. J. McMurry and R. B. Lauffer, *Chem. Rev.*, 1999, **99**, 2293.

9 M. E. Davis, Z. G. Chen and D. M. Shin, *Nat. Rev. Drug Discovery*, 2008, **7**, 771.

10 N. Lee and T. Hyeon, *Chem. Soc. Rev.*, 2012, **41**, 2575.

11 K. M. Hasebroock and N. J. Serkova, *Expert Opin. Drug Metab. Toxicol.*, 2009, **5**, 402.

12 A. Z. Khawaja, D. B. Cassidy, J. Al Shakarchi, D. G. McGrogan, N. G. Inston and R. G. Jones, *Insights Imaging*, 2015, **6**, 553.

13 N. Lee, D. Yoo, D. Ling, M. H. Cho, T. Hyeon and J. Cheon, *Therapy, Chem. Rev.*, 2015, **115**, 10637.

14 Z. Zhou, R. Bai, J. Munasinghe, Z. Shen, L. Nie and X. Chen, *ACS Nano*, 2017, **11**, 5227.

15 T.-H. Shin, Y. Choi, S. Kima and J. Cheon, *Chem. Soc. Rev.*, 2015, **44**, 4501.

16 K. H. Bae, Y. B. Kim, Y. Lee, J. Hwang, H. Park and T.G. Park, *Bioconjugate Chem.*, 2010, **21**, 505.

17 Y.-K. Peng, C. N. P. Lui, Y.-W. Chen, S.-W. Chou, E. Raine, P. -T. Chou, K. K. L. Yung and S. C. E. Tsang., *Chem. Mater.*, 2017, **29**, 4411.

18 J.-S. Choi, J.-H. Lee, T.-H. Shin, H.-T. Song, E. Y. Kim and J. Cheon, *J. Am. Chem. Soc.*, 2010, **132**, 11015.

19 T.-H. Shin, J.-S. Choi, S. Yun, I.-S. Kim, H.-T. Song, Y. Kim, K. I. Park and J. Cheon, *ACS Nano*, 2014, **8**, 3393.

20 K. Cheng, M. Yang, C. Qin, X. Su and Z. Cheng, *ACS Nano*, 2014, **8**, 9884.

21 Z. Zhou, D. Huang, J. Bao, Q. Chen, G. Liu, Z. Chen, X. Chen and J. A. Gao, *Adv. Mater*., 2012, **24**, 6223.

22 G. Huang, H. Li, J. Chen, Z. Zhao, L. Yang, X. Chi, Z. Chen, X. J. Wang and J. Gao, *Nanoscale*, 2014, **6**, 10404.

23 M. Perrier, S. Kenouche, J. Long, K. Thangavel, J. Larionova, C. Goze-Bac, A. Lascialfari, M. Mariani, N. Baril, C. Guérin, B. Donnadieu, A. Trifonov and Y. Guari, *Inorg. Chem.*, 2013, **52**, 13402.

24 V. S. Perera, L. D. Yang, J. Hao, G. Chen, B. O. Erokwu, C. A. Flask, P. Y. Zavalij, J. P. Basilion and S. D. Huang, *Langmuir*, 2014, **30**, 12018.

25 X. Cai, W. Gao, M. Ma, M. Wu, L. Zhang, Y. Zheng, H. Chen and J. A. Shi, *Adv. Mater.*, 2015, **27**, 6382.

26 L. Yang, Z. Zhou, H. Liu, C. Wu, H. Zhang, G. Huang, H. Aib and J. Gao, *Nanoscale*, 2015, **7**, 6843.

27 P. Botella, Í. Ortega, M. Quesada, R. F. Madrigal, C. Muniesa, A. Fimia, E. Fernández and A. Corma, *Dalton Trans*, 2012, **41**, 9286.

28 A. Cabrera-García, A. Vidal-Moya, Á. Bernabeu, J. Pacheco-Torres, E. Checa-Chavarria, E. Fernández and P. Botella, *Nanomaterials*, 2016, **6**, 109.

29 P. Botella, A. Corma and M. Quesada, *J. Mater. Chem.*, 2012, **22**, 6394.

30 P. K. Mascharak, *Inorg. Chem.*, 1986, **25**, 245.

31 A. M. Clemments, C. Muniesa, C. Landry and P. Botella, *RSC Adv.*, 2014, **4**, 29134.

32 A. Oyane, H.-M. Kim, T. Furuya, T. Kokubo, T. Miyazaki, T. Nakamura, *J. Biomed. Mater. Res.*, 2003, **65A**, 188.

33 S. Blüml, L. R. Schad, B. Stepanow and W. J. Lorenz, *Magn. Reson. Med.*, 1993, **30**, 289.

34 J. Hennig and H. Friedburg, *Magn. Reson. Imaging*, 1988, **6**, 391.

35 J. Hennig, A. Nauerth and H. Friedburg, *Magn. Reson. Med.*, 1986, **3**, 823.

36 M. Yamada and S. -y. Yonekura, *J. Phys. Chem. C*, 2009, **113**, 21531.

37 M. C. Navarro, E. V. Pannunzio-Miner, S. Pagola, I. Gómez and R. E. Carbonio, *J. Solid. State Chem.*, 2005, **178**, 847.

38 Y. Ding, X. Chu, X. Hong, P. Zou and Y. Liu, *Appl. Phys. Lett.*, 2012, **100**, 013701.

39 P. Botella, I. Abasolo, E. Fernández, C. Muniesa, S. Miranda, M. Quesada, J. Ruiz, S. Jr. Schwartz and A. Corma, *J. Control. Release*, 2011, **156**, 246.

40 H. B. Na, J. H. Lee, K. An, Y. I. Park, M. Park, I. S. Lee, D.-H. Nam, S. T. Kim, S.-H. Kim, S.-W. Kim, K.-H. Lim, K.-S. Kim, S.-O. Kim and T. Hyeon, *Angew. Chem. Int. Ed.*, 2007, **46**, 5397.

41 Y. Deng, E. Li, X. Cheng, J. Zhu, S. Lu, C. Ge, H. Gu and Y. Pan, *Nanoscale* 2016, **8**, 3895.

42 M. Bottrill, L. Kwoka, J. Nicholas and N. J. Long, *Chem. Soc. Rev.*, 2006, **35**, 557.

43 W. Zhang, J. Martinelli, J. A. Peters, J. M. A. van Hengst, H. Bouwmeester, E. Kramer, C. S. Bonnet, F. Szeremeta, É. Tóth and K. Djanashvili, *ACS Appl. Mater. Interfaces* 2017, **9**, 23458.

44 Y. Li, T. Chen, W. Tan and D. R. Talham, *Langmuir*, 2014, **30**, 5873.

45 T. L. Riss, R. A. Moravec, A. L. Niles, S. Duellman, H. A. Benink, T. J. Worzella, and L. Minor, Cell Viability Assays. In: *Assay Guidance Manual*; Eli Lilly & Company and the National Center for Advancing Translational Sciences, Bethesda, MD, 2012.

46 M. Mahmoudi, I. Lynch, M. R. Ejtehadi, M. P. Monopoli, F. B. Bombelli and S. Laurent, *Chem. Rev.*, 2011, **111**,5610.

47 J. Lu, M. Liong, Z. Li, J. I. Zink and F. Tamanoi, *Small*, 2010, **6**, 1794.

Graphical abstract

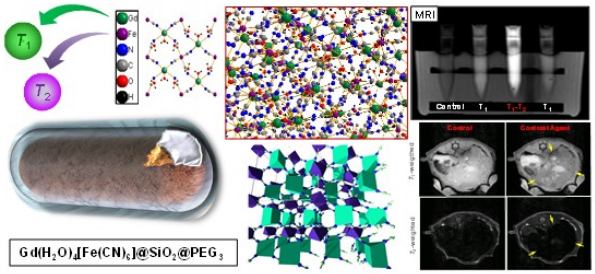

Gd and Fe centers closely packed in $Gd(H_2O)_4[Fe(CN)_6]@SiO_2$ network promote a magnetic synergistic effect, which improves longitudinal relaxivity.